Coupled strain-induced alpha to omega phase transformation and plastic flow in zirconium under high pressure torsion in a rotational diamond anvil cell

Biao Feng, Valery I. Levitas, Mehdi Kamrani

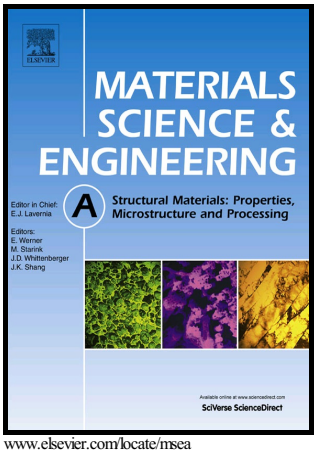

www.elsevier.com/locate/msea

PII: S0921-5093(18)30856-6
DOI: https://doi.org/10.1016/j.msea.2018.06.061
Reference: MSA36616

To appear in: *Materials Science & Engineering A*

Cite this article as: Biao Feng, Valery I. Levitas and Mehdi Kamrani, Coupled strain-induced alpha to omega phase transformation and plastic flow in zirconium under high pressure torsion in a rotational diamond anvil cell, *Materials Science & Engineering A,* https://doi.org/10.1016/j.msea.2018.06.061

Coupled strain-induced alpha to omega phase transformation and plastic flow in zirconium under high pressure torsion in a rotational diamond anvil cell

Biao Feng[1] ,Valery I. Levitas[2,3*], and Mehdi Kamrani[4]

1) Theoretical Division, Los Alamos National Laboratory, Los Alamos, NM, 87545, USA
2) Departments of Aerospace Engineering, Mechanical Engineering, and Material Science and Engineering, Iowa State University, Ames, IA 50011, USA
3) Ames Laboratory, Division of Materials Science and Engineering, Ames, IA, 50011, USA
4) Department of Aerospace Engineering, Iowa State University, Ames, IA, 50011, USA

Abstract

Strain-induced $\alpha \to \omega$ phase transformation (PT) in the zirconium (Zr) sample under compression and plastic shear in a rotational diamond anvil cell (RDAC) is investigated using the finite element method (FEM). The fields of the volume fraction of the ω phase, all components of the stress tensor, and plastic strain are presented. Before torsion, PT barely occurs. During torsion under a fixed applied force, PT initiates at the center of the sample, where the pressure first reaches the minimum pressure for strain-induced $\alpha \to \omega$ PT, p_ε^d, and propagates from the center to the periphery and from the symmetry plane to the contact surface. Salient increase of the shear friction stress and pressure at the center of a sample, so-called pressure self-multiplication effect observed experimentally for some other materials, is predicted here for Zr. It is caused by much higher yield strength of the ω phase in comparison with the α phase. Except at the very center of a sample, the total contact friction stress is equal to the yield strength in shear of the mixture of phases and the plastic sliding occurs there. Due to the reduction in sample thickness and radial material flow during torsion, the ω phase can be observed in the region where pressure is lower than p_ε^d, which may lead to misinterpretation of the experimental data for p_ε^d. For the same applied force, torsion drastically promotes PT in comparison with the compression without torsion. However, the PT process in RDAC is far from optimal: (a) due to the pressure self-multiplication effect, the pressure in the transformed region is much higher than that required for PT; (b) the region in which PT occurs is limited by the pressure p_ε^d and cannot be expanded by increasing a shear under a fixed force; and (c) the significant reduction in thickness during torsion reduces the total mass of the high-pressure phase. These drawbacks can be overcome by placing a sample within a strong gasket with an optimized geometry. It is shown that, due to strong pressure heterogeneity, characterization of $\alpha \to \omega$ and $\alpha \to \beta$ PTs based on

* Corresponding author.
Email addresses: vlevitas@iastate.edu (Valery Levitas); fengbiao11@gmail.com (Biao Feng); mkamrani@iastate.edu (Mehdi Kamrani).
LA-UR-18-23858

the averaged pressure contains large errors. The obtained results, in addition to providing an improved understanding of the strain-induced PTs, may be beneficial for the optimum design of experiments and the extraction of material parameters, as well as optimization and control of PTs by varying the geometry and loading conditions.

Keywords: Strain-induced phase transformations, Zirconium, High pressure, Rotational diamond anvil cell, Plasticity.

I. INTRODUCTION

Phase transformations (PTs) under high pressure and plastic shear are widespread in nature (e.g. as a mechanism of deep earthquakes [1-3]), physical experiments, and modern technologies. A rotational diamond anvil cell (RDAC), in which a large plastic shear in the sample without a hydrostatic medium is imposed by the rotation of anvils under a fixed axial compressive load [4-8], is utilized to study the effect of the plastic shear on PTs under high pressure. The introduction of plastic shear into the diamond anvil cell (DAC) leads to numerous exciting phenomena: (1) a significant reduction of transformation pressure by a factor of 2-5 in Refs. [8-11] and even by a factor of nearly 10 (Refs. [5,12]), in comparison with those under a hydrostatic or nearly-hydrostatic condition; (2) the substitution of reversible PTs by irreversible ones [7,8,13], which allows one to retain high-pressure phases for possible practical applications; (3) the appearance of new high-pressure phases [4,8,11,13,14], which could not be obtained without plastic shear; (4) a reduction in a transformation pressure hysteresis sometimes to zero [8,9]; (5) fast, strain-controlled rather than time-controlled kinetics, in which plastic strain plays the role of a time-like parameter [7,8,10,13].

An important point in understanding PTs under high pressure is their classification, which is introduced in [10] and [13]. When surrounded by a liquid or gaseous medium, the sample in a diamond anvil cell is under the hydrostatic condition and PTs are considered to be pressure-induced. Without hydrostatic media or above the solidification pressure of the transmitting medium, the sample is under non-hydrostatic stresses or stress tensor; PTs under nonhydrostatic conditions but below the yield strength are considered as stress-induced PTs. If PTs occur while the sample is subjected to plastic deformation, e.g. during a thickness reduction under compression in DAC or torsion in RDAC, the PTs are classified as strain-induced ones [10,13]. While pressure-induced and stress-induced PTs start at pre-existing defects, which serve as pressure and stress tensor concentrators, strain-induced PTs occur at new defects continuously created during plastic flow [10,13]. For example, dislocations as the main type of defects are generated and densely pile up at the grain boundaries or other obstacles during plastic flow, which provides a strong stress concentration. Resultant local stresses at the stress concentrators may be much higher than the applied pressure and may reach the level required for PTs, which causes a significant reduction of transformation pressure (see analytical treatment in [10,13] and phase field simulations in [15,16]) in comparison with the PT pressure under the hydrostatic

condition. Our focus here is on the plastic strain-induced PTs under pressure. Multiscale continuum thermodynamic and kinetic theories to characterize strain-induced PTs were initially proposed in [10,13]; the current state is presented in a short review in [17]. In particular, at the microscale, a plastic strain-controlled pressure-dependent kinetics (see Eq. (7)) is obtained by a coarse graining of the nanoscale theory. This kinetic equation is included in macroscale theory and used to study the coupled plastic flow and strained-induced PTs in DAC [18-21] and RDAC [22-25], using FEM.

In this paper, we will study the strain-induced PT in zirconium (Zr) from the α phase to the ω phase under compression and torsion in RDAC. Zr has widespread applications in various areas such as the space and aeronautic industry (e.g. in space vehicle parts due to its excellent resistance to heat), nuclear industry (e.g. for cladding of nuclear reactor fuels due to its low neutron-capture), and biomedical industry (e.g. dental implants and other restorative practices, knee and hip replacements, and surgical appliances, due to its high wear resistance). At normal pressure and temperature, Zr has a hexagonal closed-packed (hcp) structure (α phase). When the pressure is increased at room temperature, in the pressure range of 0.25-7 GPa [27-37], the martensitic PT from the α to ω phase occurs. With a liquid medium (4:1 ethanol:methanol), $\alpha \to \omega$ PT is observed at around 7 GPa [31], which is considered as a pressure-induced PT. With large plastic shear, plastic strain-induced $\alpha \to \omega$ PT occurs at 2 GPa [29]. While subjected to high pressure torsion (HPT) treatment under unconstrained conditions, $\alpha \to \omega$ PT is detected at 1 GPa [32] during compression before torsion; during torsion, this PT occurs at a pressure as low as 0.25 GPa [33]. The main problem in [32] and [33] is that the pressures reported are defined as the total force over the contact area, while the pressure distribution is strongly heterogeneous; see [26] and below. The initiation of $\alpha \to \omega$ PT was observed at intermediate pressures between these extremes in [29,31-33]. For instance, it occurs around 6 GPa under nonhydrostatic compression in a multi-anvil system [35]; Olinger and Jamieson obtained PT transition pressure at 3.9 GPa and suggested that the differences in PT pressure for Zr in a broad range is due to either shear stresses or oxygen content [34].

At ambient pressure as the temperature is increased from room temperature to 1135 K, the α to the bcc β PT takes place. At ambient temperature and under a hydrostatic loading, the ω phase transforms to the bcc β at 30 GPa, but the β phase is unstable and disappears after unloading. The addition of 2.5wt.% Nb to Zr causes significant decrease (at least 30 times) of the transition pressure from the α to β phase [33]. Recently, the β phase has been experimentally stabilized at normal pressure after 5 turns of the plunger at 3 GPa [38]. This pressure [38] is averaged over the contact surface as the ones in [32,33]. The stabilized β phase was later obtained by unconstrained HPT along with the ω phase at 1 GPa [32] and even 0.25 GPa [33]. While there has been significant developments in HPT (see a review [39]), and HPT is broadly used to study the PTs in Zr, the only available information is an averaged pressure (force per total initial area) and number of turns for initiation of $\alpha \to \omega$ and $\alpha \to \beta$ PTs. Thus, the system is considered as a black box. Any information on the fields of pressure, plastic strain,

and volume fraction of phases in the Zr sample during HPT, which is necessary for understanding actual physical, thermodynamic, and kinetic processes of interaction between PT and plasticity, is absent.

In our preceding paper [26], the $\alpha \to \omega$ strain-induced PT is in Zr under compression in DAC was studied. The obtained results have been utilized for the qualitative analysis interpretation of known experimental data on pressure-, stress-, and strain-induced $\alpha \to \omega$, $\alpha \to \beta$, and $\omega \to \beta$ PTs in Zr under compression and HPT, but without having a solution for HPT for Zr. In the current paper, the strain-induced $\alpha \to \omega$ PT in Zr under compression and torsion in RDAC will be studied with the same material parameters as in [26]. While there are FEM studies in RDAC [22-25], these all focus on the generic material parameters, and none are based on the real materials. Here, we performed the first study of PT in the real material (i.e. Zr) in RDAC. The results obtained will be used in comparison with those for DAC [26], to interpret the experimental phenomena, and to suggest how to improve PT conditions in RDAC.

II. PROBLEM FORMULATION

Geometry and boundary conditions

As in[26], the geometric parameters of RDAC that are generally accepted in experiments (e.g. in [5-7]) will be used in our FEM simulation. Typically, the flat [5-7] contact surface of an anvil is used for pressures under 50 GPa, while a bevel angle of 8.5^o for the anvil contact surface is used for multi-megabar pressures [41]. A flat diamond anvil is utilized (see Fig. 1c) in our model because the maximum pressure is below 5 GPa (see Fig. 2). The sample is initially pre-indented to a thickness of 50 μm at $r \le 150\,\mu$m. Due to the symmetry, a quarter of the sample and anvil structure is considered (see Fig. 1a). To avoid divergence of the computations due to the penetration of finite elements between diamond and sample if the sharp angle at point *C* is used, a smooth corner is included in the geometric schematic (see Fig. 1b).

The boundary conditions for a quarter of a structure in Fig. 1a are as follows:

(1) The normal stress σ_n is applied at the top surface of the anvil. In the course of torsion, the rotation is applied to the top surface of the anvil with a constant normal stress σ_n.

(2) The radial displacement u_r and shear stresses τ_{rz} and $\tau_{z\varphi}$ are zero at the symmetry axis $r = 0$ (the lines *AB* and *BG* for the anvil and the sample, respectively).

(3) At the contact surface between the anvil and sample (the line *BCD*), the combined Coulomb and plastic friction model, which will be introduced below in this section, is used.

(4) At the symmetry plane $z = 0$ (the plane *GH*), the radial shear stress $\tau_{rz} = 0$, and the circumferential displacement and the axial displacement are both zero $u_\varphi = u_z = 0$.

(5) Other surfaces in Fig. 1a not mentioned above are stress-free.

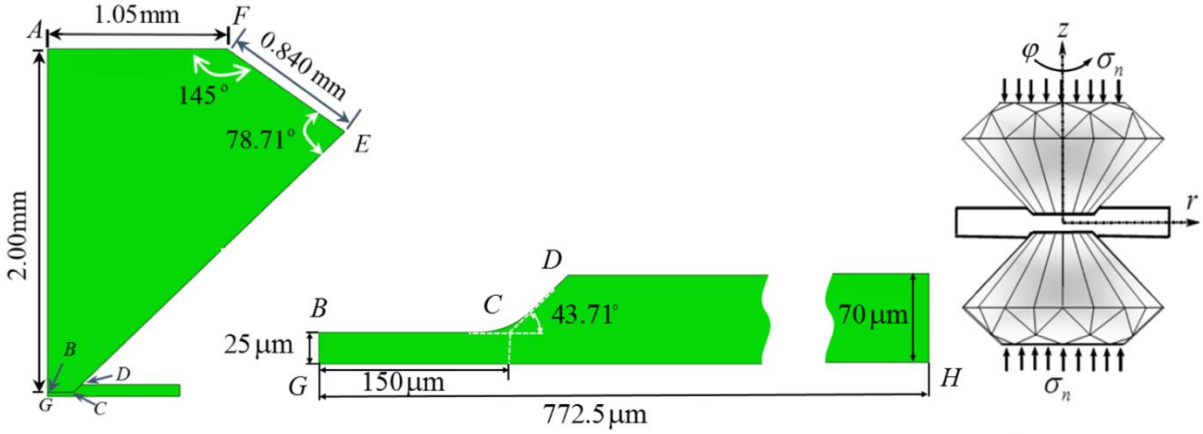

(a) (b) (c)

FIG. 1. (a) A quarter of the sample and the anvil in the initial undeformed state with the geometric parameters, (b) the geometry of a quarter of the sample, (c) a RDAC schematic.

Material model

It was found in [42] for a wide range of materials (metals, rocks, pressed powders, etc.) that above some level of plastic strain, initially isotropic polycrystalline materials deform as perfectly plastic and isotropic; their yield surface is independent of accumulated plastic strain and plastic strain history. Because the maximum pressure is around 5 GPa, we can also neglect the pressure dependence of the elastoplastic properties (similar to [22-26,37]). Thus, isotropic and perfectly plastic behavior with the von Mises yield condition is assumed for the Zr sample. The elastic properties and yield strength are considered to be phase-volume-fraction-dependent. The model for Zr here is basically identical to the 2D model in [26] but will be used for more general 3D loading. A system of equations considering coupled elasto-plasticity and strain-induced PT is summarized as follows.

Kinematic decomposition of the symmetric part of the velocity gradient $\mathbf{d}$:

$$\mathbf{d} = \left(\dot{\mathbf{F}} \cdot \mathbf{F}^{-1}\right)_s = \overset{\nabla}{\boldsymbol{\varepsilon}}_e + \frac{1}{3}\dot{\varepsilon}_t \mathbf{I} + \mathbf{d}_p, \quad \varepsilon_t = \bar{\varepsilon}_t c \tag{1}$$

Where $\overset{\nabla}{\boldsymbol{\varepsilon}}_e$ is the objective Jaumann time derivative of the elastic strain; $\mathbf{I}$ is the second-rank unit tensor; $\bar{\varepsilon}_t$ is the transformation volumetric strain for a complete PT; and c is the volumetric fraction of the high-pressure (ω) phase.

Hooke's elasticity law:

$$\boldsymbol{\varepsilon}_e = \frac{1}{E}\left[\boldsymbol{\sigma} - \upsilon\left(\mathrm{tr}\left(\boldsymbol{\sigma}\right)\mathbf{I} - \boldsymbol{\sigma}\right)\right], \quad \mathrm{tr}\left(\boldsymbol{\sigma}\right) = \sigma_{rr} + \sigma_{zz} + \sigma_{\varphi\varphi} \tag{2}$$

Where Young's modulus $E = (1-c)E_1 + cE_2$ and Poisson's ratio $\upsilon = (1-c)\upsilon_1 + c\upsilon_2$; in this paper, subscripts 1 and 2 represent the low- and high-pressure phases, respectively.

Von Mises yield condition for a two-phase mixture:

$$\sigma_i = \left(\frac{3}{2}\mathbf{s}:\mathbf{s}\right)^{0.5} \le \sigma_y(c) = (1-c)\sigma_{y1} + c\sigma_{y2}, \tag{3}$$

Where **s** is the deviator of the Cauchy stress $\boldsymbol{\sigma}$.

J_2 flow rule in the plastic region:

$$\sigma_i = \sigma_y(c), \qquad \mathbf{d}_{\mathrm{p}} = \lambda \mathbf{s}, \qquad \lambda \ge 0 \tag{4}$$

in the elastic region:

$$\sigma_i \le \sigma_y(c), \qquad \mathbf{d}_{\mathrm{p}} = 0 \tag{5}$$

Where σ_i is the effective stress and λ is a parameter that is determined by iterative satisfaction of the yield condition.

Equilibrium equation:

$$\nabla \cdot \boldsymbol{\sigma} = 0, \tag{6}$$

In the micro-scale theory [10,13], the strain-controlled kinetic of strain-induced PTs can be characterized as:

$$\frac{dc}{dq} = 10k \frac{(1-c)\bar{p}_d H(\bar{p}_d)\dfrac{\sigma_{y2}}{\sigma_{y1}} - c\bar{p}_r H(\bar{p}_r)}{c + (1-c)\dfrac{\sigma_{y2}}{\sigma_{y1}}}, \tag{7}$$

where k is the kinetic parameter; $\bar{p}_d = \dfrac{p - p_\varepsilon^d}{p_h^d - p_\varepsilon^d}$ and $\bar{p}_r = \dfrac{p - p_\varepsilon^r}{p_h^r - p_\varepsilon^r}$ are the dimensionless characteristic pressures for direct and reverse PTs; p_ε^d is the minimum pressure below which direct strain-induced PT (direct indicates the PT from low-pressure to high-pressure phase) is impossible; p_ε^r is the maximum pressure above which reverse strain-induced PT (reverse indicates the PT from high-pressure to low-pressure phase) cannot occur; p_h^d and p_h^r are the pressures for direct and reverse PTs under the hydrostatic condition, respectively; H is the Heaviside step function; and q is the accumulated plastic strain, defined as $\dot{q} = (2/3\mathbf{d}_p : \mathbf{d}_p)^{1/2}$.

Friction model

In the Coulomb friction model, no relative displacement will occur between surfaces in contact as long as the friction stress τ is smaller than the critical friction stress defined as $\tau_{crit} = \mu\sigma_c$, where μ is the friction coefficient and σ_c is the normal contact stress. This critical friction stress should be redefined for the elastoplastic materials because, when the magnitude of the friction stress τ reaches the yield strength in shear, τ_y (e.g. $\tau_y = \sigma_y/\sqrt{3}$ in the von Mises yield criterion), relative slipping can occur even if $\tau < \mu\sigma_c$. In this paper, the critical friction stress is defined as $\tau_{crit} = \min\left(\mu\sigma_c, \tau_y(c)\right)$ and μ is considered to be constant for the simplest

case. Yield strength in shear is considered to be dependent on PT evolution as $\tau_y(c)=(1-c)\tau_{y1}+c\tau_{y2}$, where τ_{y1} and τ_{y2} are the yield strengths in shear of the low- and high-pressure phases, respectively. In the generalized axisymmetric models, the three-dimensional friction stress $\boldsymbol{\tau}$ along the contact surface is composed of τ_{rz} along the radial direction and $\tau_{\phi z}$ along the circumferential twist direction as $\tau=|\boldsymbol{\tau}|=\left(\tau_{rz}{}^2+\tau_{\varphi z}{}^2\right)^{0.5}$.

Redefinition of the critical friction stress as $\tau_{crit}=\min\left(\mu\sigma_c,\tau_y(c)\right)$ results in a sudden change of contact conditions between cohesion and sliding. This may cause convergence issues in the FEM methods in the iterative process, especially for our model, where a large slipping can happen. Hence, to mitigate this problem, a small elastic reversible tangential slip u_e is substituted for the cohesion condition [43]. In other words, the contact relative displacement is decomposed into elastic (reversible) sliding u_e and plastic (irreversible) slipping u_s as $u_c=u_e+u_s$. The elastic sliding can be physically interpreted as the elastic deformation of the thin contact layer, while slipping corresponds to the plastic flow in this layer. In this paper, u_{crit} is considered to be equal to 0.5% of the average element length for the fine-mesh discretization.

In this paper, a linear relation $\tau=k_s u_e$, where k_s is the contact stiffness, is considered. The contact stiffness can be determined from $\tau_{crit}=k_s u_{crit}$ to be $k_s=\tau_{crit}/u_{crit}$. Therefore, k_s depends on the normal stress σ_n and the yield strength in shear τ_y. The complete system of equations for the combined Coulomb and plastic friction is as follows:

Decomposition of contact relative displacement into elastic sliding and irreversible slipping:

$$\mathbf{u}_c=\mathbf{u}_e+\mathbf{u}_s, \tag{8}$$

Critical shear stress:

$$\tau_{crit}=\min\left(\mu\sigma_c,\tau_y(c)\right), \tag{9}$$

Yield strength in shear:

$$\tau_y(c)=(1-c)\tau_{y1}+c\tau_{y2}, \tag{10}$$

Elastic sliding vector:

$$\begin{cases}\mathbf{u}_e=\dfrac{u_{crit}}{\mu\sigma_c}\boldsymbol{\tau}, & if \quad \mu\sigma_c<\tau_y(c)\\ \mathbf{u}_e=\dfrac{u_{crit}}{\tau_y(c)}\boldsymbol{\tau}, & if \quad \mu\sigma_c\geq\tau_y(c)\end{cases} \tag{11}$$

Sliding rule:

below the critical shear stress:

$$|\dot{\mathbf{u}}_s|=0, \qquad if \quad \tau=|\boldsymbol{\tau}|=\left(\tau_{rz}{}^2+\tau_{\varphi z}{}^2\right)^{0.5}<\tau_{crit} \tag{12}$$

at the critical shear stress:

$$\begin{cases} \dot{\mathbf{u}}_s = \dfrac{|\dot{\mathbf{u}}_s|}{\mu\sigma_c}\,\boldsymbol{\tau}, & if \quad \mu\sigma_c \le \tau_y(c) \\ \dot{\mathbf{u}}_s = \dfrac{|\dot{\mathbf{u}}_s|}{\tau_y(c)}\boldsymbol{\tau}, & if \quad \mu\sigma_c > \tau_y(c) \end{cases} \tag{13}$$

Material parameters and numerical procedure

The material parameters used for diamond and Zr in this paper are the same as those used in [26]. The diamond is considered as an isotropic elastic material with the bulk modulus *B* and Young's modulus *E* of 443 GPa [44] and 1048.5 GPa [45], respectively. Therefore, based on Hooke's law, Poisson's ratio υ is 0.1055. The Young's modulus, Poisson's ratio, [46] and yield strength [47] for Zr phases are as follows:

For the α phase: $E_1 = 90.9\,\text{GPa}$, $\upsilon_1 = 0.344$ and $\sigma_{y1} = 180$ MPa

For the ω phase: $E_2 = 113.8\,\text{GPa}$, $\upsilon_2 = 0.305$ and $\sigma_{y2} = 1180$ MPa

The transformation pressures for pressure- and strain-induced PTs strongly depend on impurities such as elements of oxygen and nitrogen [30], the initial mechanical state of the material, and the measurement conditions. As discussed in the Introduction, there is an essential scatter of transformation pressures in literature. Significant corrections to the PT pressures in [33] were suggested in [26] due to operating by the averaged pressure (force per unit initial area) while the pressure distribution is strongly heterogeneous. We use p_ε^d=1.7 GPa and p_ε^r=-2 GPa for direct and reverse strain-induced PTs, respectively. For pressure-induced PTs, we accept p_h^d =7 GPa and p_h^r=-3.7 GPa for direct and reverse strain-induced PTs, respectively. The kinetic parameter is considered *k*=10. Based on the experimental data given in [48], the transformational volumetric strain is $\bar{\varepsilon}_t = -0.014$.

ABAQUS FEM code [43] was used in our simulations. To solve the strain-controlled kinetics Eq. (7), the ABAQUS user subroutines [43] USDFLD and HETVAL are used. In these subroutines, the thermal strain and temperature are treated as transformation strain and the volume fraction of high-pressure phase *c*, respectively. To implement the friction model defined in Sec. II, the user subroutine FRIC [43] in ABAQUS is used.

III. STUDY OF COUPLED PLASTIC FLOW AND PHASE TRANSFORMATIONS

III.1 Distribution of the pressure and volume fraction of the ω phase

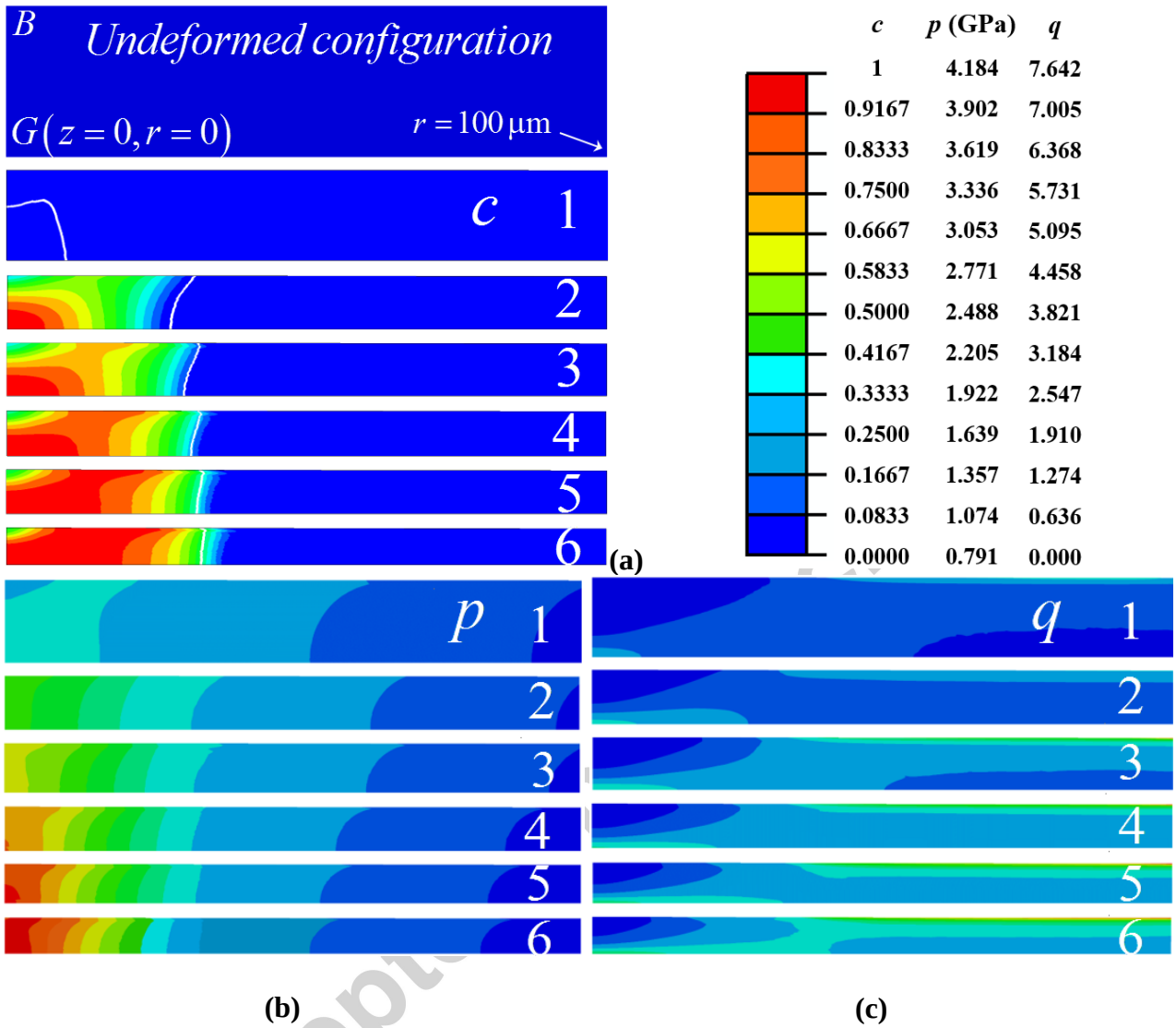

FIG. 2. Distributions of the volume fraction *c* of the high-pressure ω phase of Zr (a), pressure *p* (b), and accumulated plastic strain *q* (c), for $0 \le r \le 100\,\mu\text{m}$, before and during torsion under the applied constant stress σ_n =27.6 MPa. Designations of the rotation angles: 1: φ =0.0; 2: φ =0.16; 3: φ =0.32; 4: φ =0.48; 5: φ =0.64; and 6: φ =0.8 radians. The white line in (a) corresponds to the pressure equal to p_{ε}^{d}.

In this section, we will discuss the plastic flow and strain-induced $\alpha \rightarrow \omega$ PT in Zr during torsion under a fixed axial compressive load. Fig. 2 presents the evolutions of the volume fraction *c* of the ω phase of Zr, pressure *p*, and accumulated plastic strain *q* in the part of the Zr sample for $0 \le r \le 100\,\mu\text{m}$ with a rising rotation angle.

The applied compressive stress on the top surface of the upper anvil is σ_n =27.6 MPa, as shown in Fig. 1c. If the resultant force is divided by the area of the flat surface of an anvil, an averaged

pressure on the sample surface is $0.0276*\left(1.05/0.15\right)^2=1.35$ GPa. Because there is an additional inclined contact surface between the diamond and the sample, it should be even smaller. If we consider the horizontal area with radius corresponding to point D, the mean pressure is $0.0276*\left(1.05/\left(0.15+.047\right)\right)^2=0.784$ GPa.

The white lines in Fig. 2a correspond to pressure $p=p_\varepsilon^d$, which is the minimum pressure for strain-induced PTs to the high-pressure phase, and on the left and right sides of these lines, pressures are higher and lower than p_ε^d, respectively. Fig. 2a shows that the sample thickness reduces significantly when the sample is compressed under σ_n =27.6 MPa without rotation, leading to a plastic deformation in the entire sample. Although the pressure at the center is higher than the minimum pressure for $\alpha\rightarrow\omega$ PT, p_ε^d, the volume fraction of the ω phase there is lower than 0.0883; therefore, the PT is not visible and the color of the volume fraction in the entire sample is dark blue. With such a small volume fraction, the ω phase should not be detected in an experiment under compression either. This is consistent with experiments in [33] because an averaged pressure here, 0.784 GPa, is smaller than 1 GPa, at which the ω phase was not detected under compression. The phase transformation starts at the center of the sample, where the pressure reaches the p_ε^d first, and it propagates from the center to the periphery with an increase in rotation angle as the white line with a pressure of p_ε^d moves to the periphery. During rotation, the thickness of the sample significantly reduces, causing an increase of the pressure gradient due to the simplified equilibrium equation

$$\partial p/\partial r=2\tau_{rz}^c/h \tag{14}$$

where *h* is the sample thickness and τ_{rz}^c is the friction shear stress on the contact surface in the radial direction. Another reason for a rising pressure gradient in the transforming region is the increase in shear stress τ_{rz} (see τ_{rz} in Fig. 6a or 7a) due to material hardening during PT. Fig. 2c presents the evolution of the plastic strain *q*. Because the plastic shear strain is large near the contact surface at the periphery of a sample, the maximum plastic strain is localized there as well (see fig. 2c). At *r*=0, the shear stress and strain are zero, and thickness reduction in this region is mostly caused by the radial flow of material near the symmetry plane. Small plastic straining near the contact surface at the sample center leads to a slow PT rate there (Eq. (7)). According to Figs. 2a and 3, for compression before torsion under the applied normal stress of σ_n =27.6 MPa, there is be no detectable PT near the contact surface, and there is only a small region of a slightly transformed phase at the center of the sample. However, during torsion under the same normal stress, PT evolves and completes in a large region of the sample which includes the contact surface.

Fig. 3 plots the pressure and the volume fraction of the high-pressure phase along the contact surface. Due to the symmetry, the pressure gradient is zero at the center-line *z* axis. In the untransformed region at the periphery, the pressure gradient is almost constant because the friction shear stress τ_{rz} (see in Fig. 7c) in Eq. (14) is constant. The pressure gradient in the two-phase region increases because the yield strength increases with the volume fraction *c*, which, in turn, varies along the contact surface. The increase in pressure and the pressure gradient during the rotation shown under constant applied force in Fig. 3 is caused by friction stress growth during phase transformation and thickness reduction during material radial flow. This was observed in experiments on different materials [8, 9, 11] and referred to as the pressure self-multiplication effect. Thus, our prediction of the pressure self-multiplication effect in Zr has conceptual confirmation for PTs in KCl and fullerene [8, 9, 11]. In return, this increase in pressure intensifies the PT rate in this region; see Eq. (7). While the pressure reaches its maximum in the central region of the contact surface, the volume fraction of the ω phase in this region is relatively small due to the relatively small plastic deformation in this region. With an increasing rotation angle, there is a significant material flow from the center to the periphery and, consequently, a significant thickness reduction. During this radial material flow, the two-phase zone flows into the region with pressure lower than p_ε^d. According to Figs. 2a and 3, the ω phase can be found in the region where pressure is lower than p_ε^d; there, the PT cannot occur. If p_ε^d is defined as the minimum pressure in the transformed region, this may lead to significant misinterpretation of experiments.

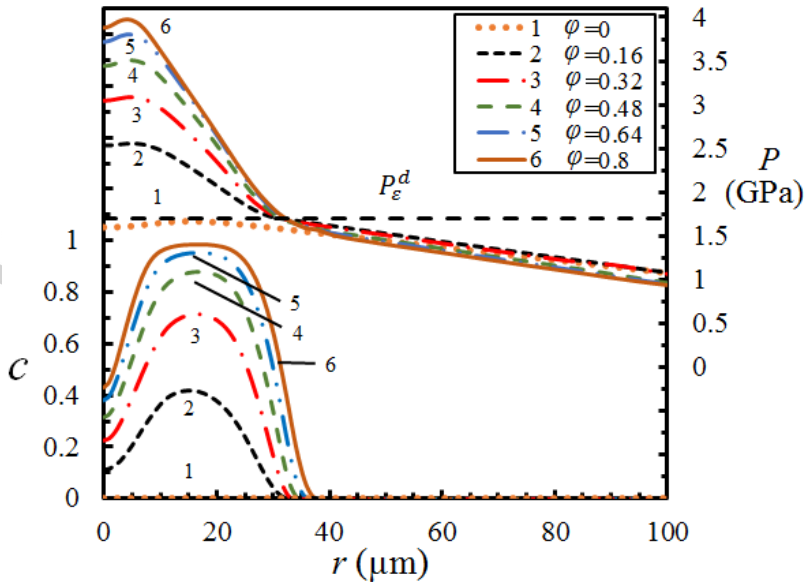

FIG. 3. Distributions of volume fraction *c* of the high-pressure phase and pressure *p* at the contact surface between diamond and sample for $0 \le r \le 100\,\mu\text{m}$ before and during torsion

under the applied constant normal stress σ_n =27.6 MPa. 1: φ =0.0, 2: φ =0.16, 3: φ =0.32, 4: φ =0.48, 5: φ =0.64, 6: φ =0.8 radians.

As in traditional in HPT, the averaged pressure is used to describe the pressure for PT and it is from the total applied compressive force divided by the contact surface. At room temperature, the martensitic PT from the α to ω phase occurs and is reported in the pressure range of 0.25-7 GPa [27-37], among which HPT is mostly used.

Similar to the PT under compression in DAC [26], in RDAC Fig. 3 demonstrates that PT cannot be characterized by the averaged pressure, as this was done in all previous experimental papers (e.g., [32,33,36]). During torsion at a constant averaged pressure, the maximum pressure grows from 1.8 GPa to 4.0 GPa in Fig. 10 while average pressure (0.784 GPa) does not change, i.e. by a factor of 2.2. It is slightly larger than a factor of 2, which was estimated for DAC in [26]. While the geometry of a sample in RDAC differs from that in HPT, some qualitative conclusions should be the same. During compression, the minimum pressure for the strain-induced PT p_ε^d =1.7 GPa is reached at the averaged pressure of 0.784 GPa, which is 2.2 times lower. It is lower than the upper bound of 3, estimated in [26], due to the effect of the inclined part of the sample, which is absent in HPT. This multiplier 3 was used in [26] to correct the magnitude of p_ε^d for $\alpha \to \omega$ PT based on the averaged pressure in [32,33]. The maximum pressure after torsion exceeds an averaged pressure of 0.784 GPa by a factor of 5. This factor should be used to correct the minimum pressure for strain-induced PT p_ε^d for $\alpha \to \beta$ transformation based on the averaged pressure in [32,33]. Strong heterogeneity in all fields and difference in geometric conditions (which are very seldom specified), is one of the important sources of explanation of the strong scatter in transformation pressures for $\alpha \to \omega$ PT in Zr in [27-37].

Rotation above some critical angle is not effective. The amount of high-pressure phase cannot grow anymore because the region with pressure larger than p_ε^d is limited and PT is almost completed in it. Also, the thickness of a sample reduces with rotation, the high-pressure phase flows to the region where $p < p_\varepsilon^d$, and reverse PT occurs. Increasing the applied normal stress σ_n is a way to increase the span of the transformed region. Fig. 4 shows the distributions of the volume fraction of the high-pressure phase and pressure in the sample for three different applied normal stresses for the rotation angle φ =0.8. The span of the transformed region increases and PT advances further at the center of the contact surface when the applied normal stress increases from 27.6 MPa to 28.1 MPa and to 28.6 MPa, which correspond to the final thicknesses of 12.6 μm, 12.18 μm, and 11.94 μm, respectively.

If the same stresses σ_n were applied to the DAC without torsion, PT would not even reach the contact surface. Therefore, superposing torsion in the RDAC significantly reduces the normal force, i.e. the averaged pressure, for having a large transformed region. Reduction in

force also reduces normal stresses and deformations in the anvils. Therefore, the RDAC is preferable over the DAC in high-pressure experiments.

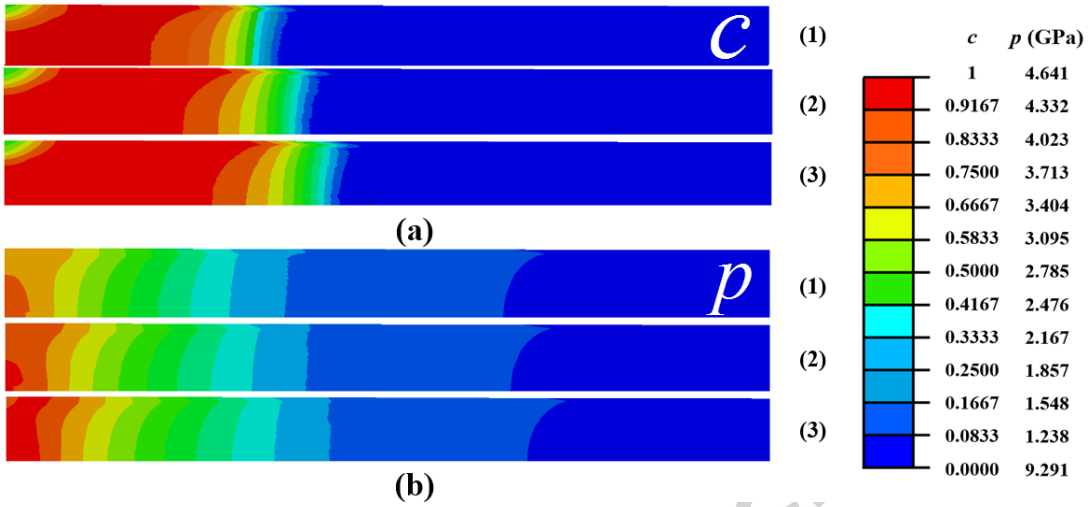

FIG. 4. (a) Distributions of the volume fraction c of the ω phase and (b) pressure p for $0 \le r \le 100\,\mu\text{m}$, under applied constant normal stress σ_n =27.6 MPa (1) , σ_n =28.1 MPa (2), and σ_n =28.6 MPa (3) after a rotation of φ =0.8 radian.

Despite the advantages in the PT process in RDAC compared to those in DAC, there are clear drawbacks. Thus, pressure in the transformed region is much higher than the minimum PT pressure p_ε^d. Such a pressure is not required for PT but could not be avoided for the geometry under consideration. Second, the region in which PT occurs is limited by the condition $p > p_\varepsilon^d$ and cannot be increased by increasing shear under fixed force. Third, significant reduction in thickness during torsion reduces the total mass of the high-pressure phase. Fourth, the transformed material can flow to the region with $p < p_\varepsilon^d$ during rotation; then the reversed PT may, in principle, occur. The way to overcome these drawbacks is to use the sample within a strong gasket, optimize the geometric parameters of the gasket, and achieve nearly-homogeneous pressure distribution within the sample, which does not change obviously during torsion and PT. After a simplified analytical optimization, this was demonstrated in experiments for PT from hexagonal to superhard wurtzitic boron nitride [7]. This was later achieved in FEM simulations in RDAC [23].

III.2 Distribution of the normal and shear stresses

Fig. 5 presents the evolution of the distribution of the normal stresses σ_{rr}, σ_{zz}, and $\sigma_{\varphi\varphi}$ in the sample before and during rotation. The distributions of σ_{rr} and $\sigma_{\varphi\varphi}$ are almost identical. Because the deviation of σ_{zz} from σ_{rr} and $\sigma_{\varphi\varphi}$ is limited by the yield strength, the general tendency in the evolution of normal stresses in Fig. 5 is close to that for pressure evolution in Fig.

2c. At the center, all normal stresses and their radial gradients significantly increase with a rising rotation angle due to material hardening during PT and the thickness reduction during material radial flow. Stress σ_{zz} is nearly unchanged along the thickness, excluding the very central part of the sample. In contrast, σ_{rr} and $\sigma_{\varphi\varphi}$ reduce along the sample thickness due to the reduction of the shear stress τ_{rz} from the maximum at the contact surface to zero at the symmetry plane (See Fig. 6). Thus, the magnitude of the difference $\sigma_{zz}-\sigma_{rr}$ (and $\sigma_{zz}-\sigma_{\varphi\varphi}$) should increase from the contact surface to the symmetry plane to satisfy the yield condition.

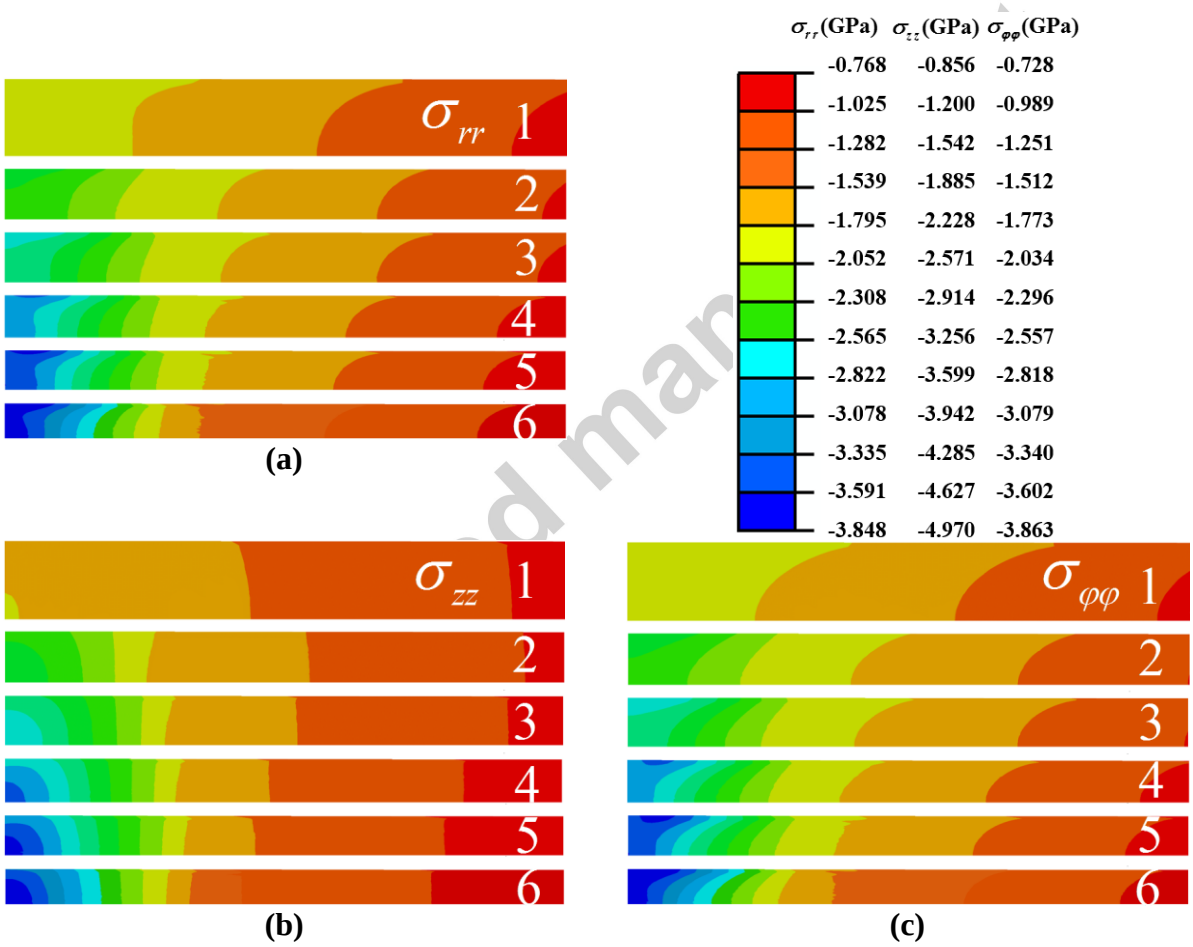

FIG. 5. Distributions of normal stresses σ_{rr} (a), σ_{zz} (b), and $\sigma_{\varphi\varphi}$ (c) in the sample for $0 \le r \le 100\,\mu m$ before and during torsion under the applied constant normal stress σ_n =27.6 MPa. 1: φ =0.0, 2: φ =0.16, 3: φ =0.32, 4: φ =0.48, 5: φ =0.64, 6: φ =0.8.

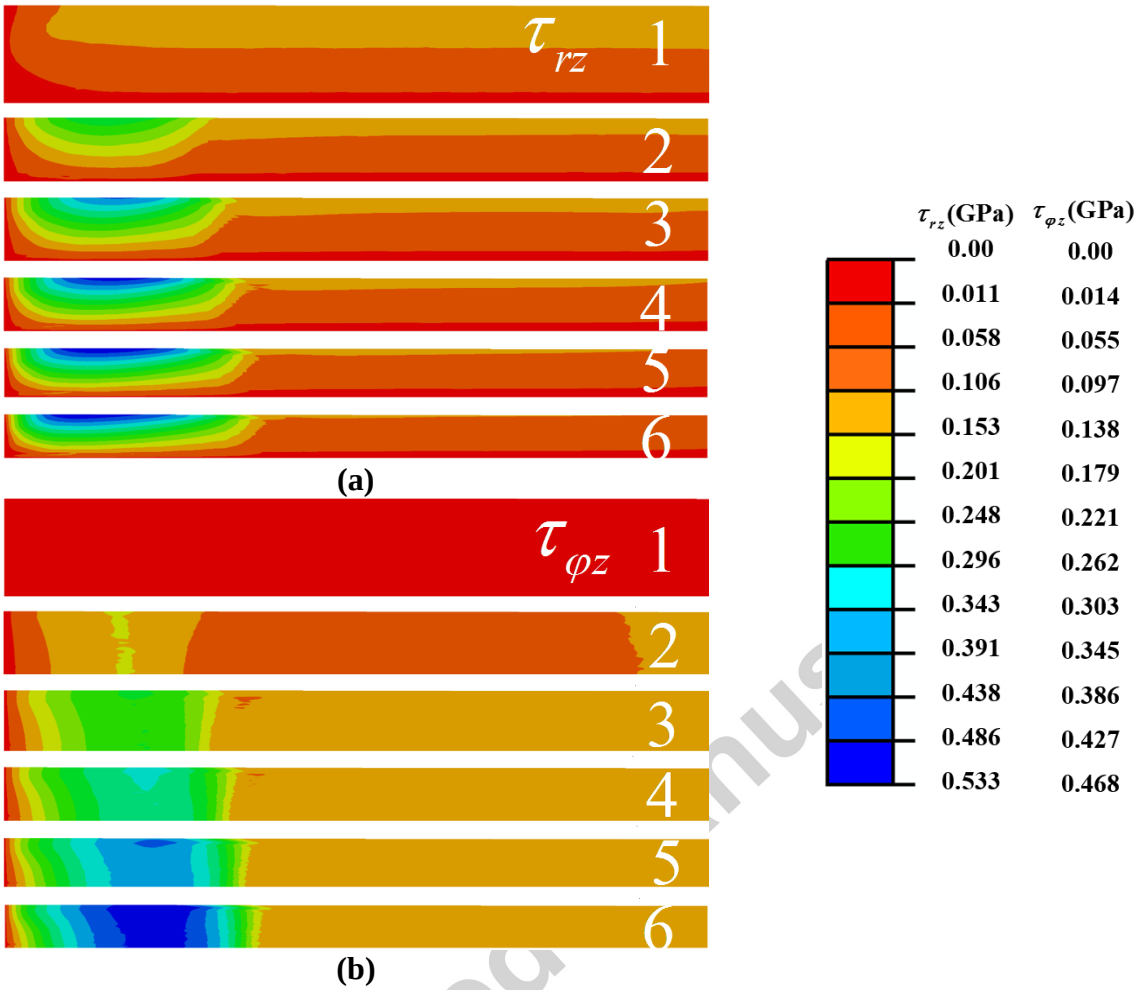

FIG. 6. Distribution of shear stresses τ_{rz} (a) and $\tau_{\varphi z}$ (b) in the sample for $0 \le r \le 100\,\mu$m before and during torsion under the applied constant normal stress σ_n =27.6 MPa. 1: φ=0.0, 2: φ=0.16, 3: φ=0.32, 4: φ=0.48, 5: φ=0.64, 6: φ=0.8.

The evolution of shear stresses τ_{rz} and $\tau_{\varphi z}$ in the sample during torsion is presented in Fig. 6. Due to symmetries, the radial shear stress τ_{rz} at the symmetry plane (z=0) and at the symmetry axis (r=0) is zero. It increases from the symmetry plane to the contact surface, where it reaches its maximum. Distinct from τ_{rz} with a large gradient along the thickness, the circumferential shear stress $\tau_{\varphi z}$ is almost unchanged along the thickness. During PTs, material hardening, which increases with an increasing volume fraction c, induces an increase in the shear stresses and their gradient in the transformed region. During compression before torsion, τ_{rz} reaches the yield stress in shear of the α phase in the major part of the contact surface (Fig. 7), which causes a constant pressure gradient in Fig. 2. During torsion, $\tau_{\varphi z}$ increases, causing the reduction of τ_{rz} to maintain the total shear stress at the contact surface $\tau = \left(\tau_{rz}^{\,2} + \tau_{\varphi z}^{\,2}\right)^{0.5}$ equal to the yield

strength in shear. The total shear stress reaches about 6.5 times the yield strength in shear of the α phase in the nearly fully-transformed region in Fig. 7, which is close to the ratio of the yield strengths of the ω and α phases. In the major region, except at the center of a sample, the τ is equal to the yield strength in shear, indicating that the plastic sliding is allowed there (see Fig. 7).

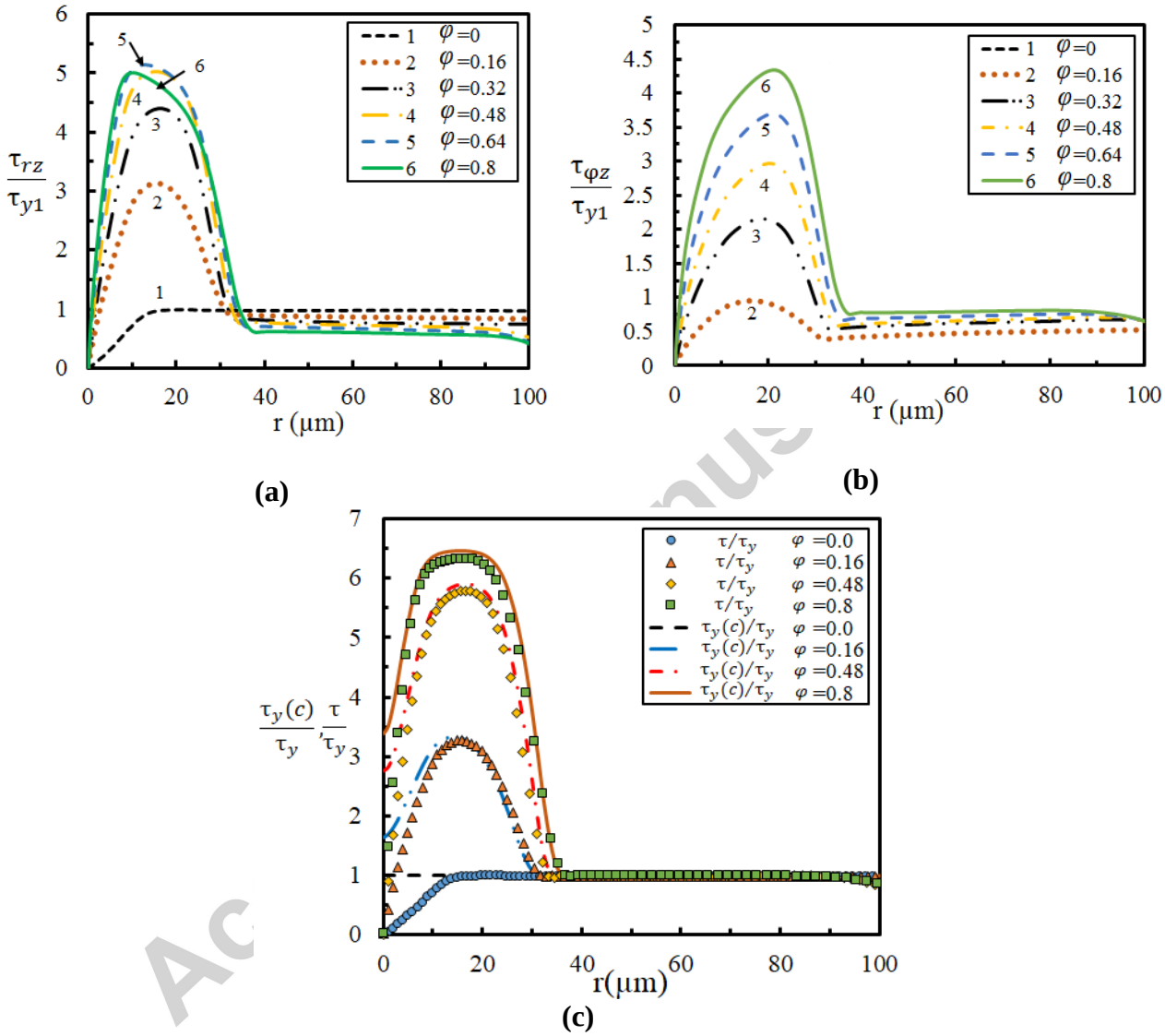

FIG. 7. Distributions of dimensionless friction shear stresses τ_{rz}/τ_{y1} (a) and $\tau_{\varphi z}/\tau_{y1}$ (b), yield stress in shear $\tau_y(c)/\tau_{y1}$, and total shear stress τ/τ_{y1} (c) at the contact surface of the sample for $0 \le r \le 100\,\mu\text{m}$, before and during torsion under the applied constant normal stress σ_n =27.6 MPa. In (a) and (b), 1: φ =0.0, 2: φ =0.16, 3: φ =0.32, 4: φ =0.48, 5: φ =0.64, 6: φ =0.8.

III. 3. Contact sliding, deformation of an anvil, and reduction in sample thickness

The relative radial displacement d and relative circumferential rotation angle β between the sample and the diamond anvil at the contact surface is shown in Figs. 8a and 8b, respectively. Fig. 8 shows that the radial and circumference slip exists everywhere except the central region of the contact surface, where the cohesion condition holds. Material flows from the center to the periphery, and the slope of radial slip displacement d increases with an increase in the radial coordinate. The tendencies of the relative radial displacement d and relative circumferential rotation angle β are very similar. The relative circumferential rotation angle β is defined as $\beta = \beta_{diamond} - \beta_{sample}$, in which $\beta_{diamond}$ (or β_{sample}) is the rotation angle of diamond (or sample) with respect to the symmetric plane (z=0). Initially, before the rotation starts, β is zero everywhere at the contact surface. With the rotation angle φ=0.16 radians, Fig. 8b shows that the cohesion zone between the diamond and sample surface is localized in the region of $r \le 20\,\mu m$, and beyond the this region, the relative circumferential rotation β increases with a rising radial coordinate. At the periphery, the circumferential sliding is larger than that at the center, which is caused by a lower contact stress σ_c at the periphery and a larger circumferential displacement of the anvil at the periphery. In addition, with the increase of the rotation angle φ, the cohesion region decreases and β increases at the non-cohesion zone. Fig. 7 shows that the friction stress is equal to the yield strength in shear in most of the contact region, which means that the plastic sliding occurs almost everywhere at the contact surface. This result shows the importance of taking plastic sliding along the contact surface into account. Without this plastic friction condition, radial and circumferential sliding would be suppressed, the sample thickness would be artificially increased, and the pressure distribution would be changed as well.

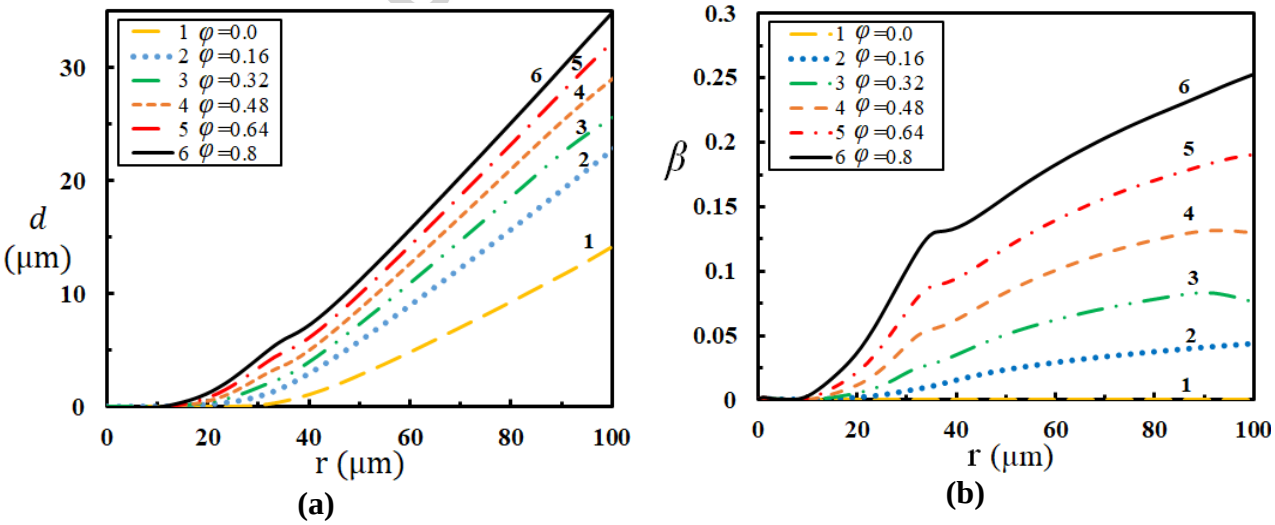

FIG. 8. Distributions of radial d (a) and relative circumferential rotational angle β (b) between the sample and the diamond anvil at the contact surface for $0 \le r \le 100\,\mu m$ before and

during torsion under applied constant normal stress σ_n =27.6 MPa, 1: φ =0.0, 2: φ =0.16, 3: φ =0.32, 4: φ =0.48, 5: φ =0.64, 6: φ =0.8.

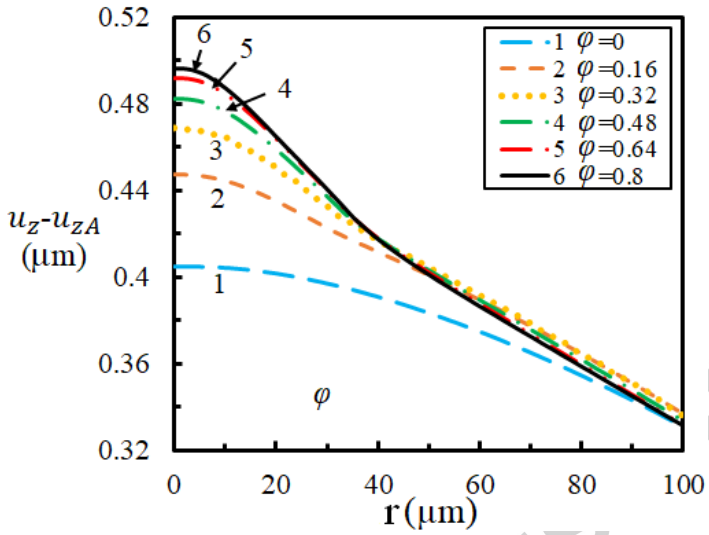

FIG. 9. Relative *z*-displacement of the points of the contact surface with respect to the point C in Fig. 1a with increasing anvil rotation, i.e. evolution of the deformed profile of the diamond-sample contact surface.

As mentioned, although diamond is very rigid (the Young's modulus of diamond is 1045.5 GPa, which is 11.5 and 9.2 times larger than those of the α and ω phases, respectively) and the maximum normal stress is below 4 GPa, because the contact surface of the diamond with the sample is long compared to the final thickness of the sample, the bending of a diamond anvil cannot be neglected. Fig. 9 shows the evolution of the deformed profile of the diamond-sample contact surface.

The maximum deformation of an anvil along the symmetry axis reaches 0.4 μm after compression before torsion and increases from 0.4 to 0.5 μm during torsion due to redistribution of the contact stresses. As the contact normal stress becomes larger at the center of the sample (see Fig. 2) and slightly smaller at the periphery, the evolution of the deformation of the anvil repeats this trend. Moreover, there is a change in the pressure gradient at the broad interface between transformed and non-transformed regions (see Fig. 3), which coincides with a slight change in the slope of the diamond contact surface profile at this point. The final thickness of the sample at the center-line for a rotation angle of 0.8 and applied σ_n =27.6 MPa is around 12.6 μm , and Fig. 9a gives the thickness of the sample at the periphery (*r*=100) 0.32 μm $(2\times 0.16\,\mu\text{m})$, or 2.5% smaller.

The variation of the sample thickness h at the symmetry axis (r=0) and the maximum dimensionless pressure $p_{\max}/\sigma_{y1}$ in the sample during rotation is shown in Fig. 10. Under compression, the sample thickness reduces to 28.61 μm. The slope of the thickness reduction is large at the initial stage of rotation and decreases as the rotation angle increases. This is qualitatively consistent with the analytical solution for torsion under a fixed load without PT [10,13]. In addition, because the yield strength increases during PT, this also suppresses thickness reduction. Fig. 10 also shows that, during torsion, the maximum pressure increases due to the increase in the yield strength and friction stress during PTs. Note that without PT, the pressure distribution does not change during torsion, which has been obtained analytically [10,13], numerically, [49] and experimentally [8,11].

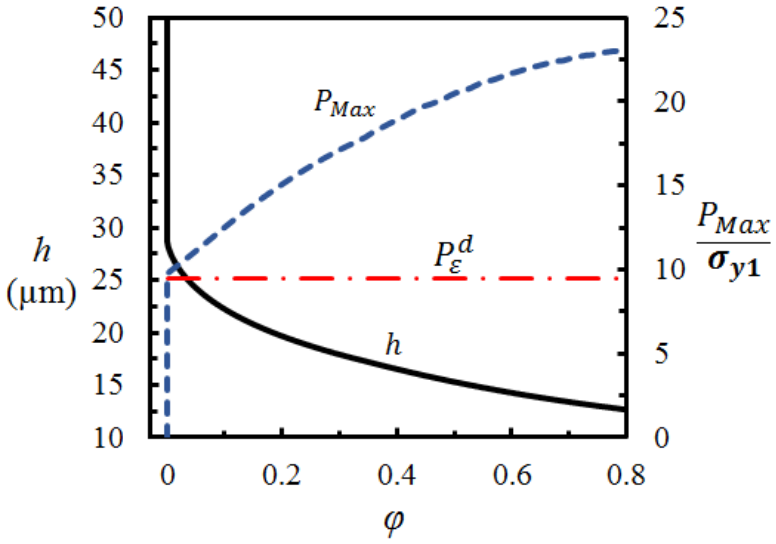

FIG. 10. The variations of the sample thickness h and the dimensionless maximum pressure $p_{\max}/\sigma_{y1}$ in the sample during torsion under applied constant normal stress σ_n =27.6 MPa.

IV. CONCLUDING REMARKS

The main problem in studying the PTs during HPT with metallic anvils for all materials with RDAC for most materials including Zr is that the only available information is the averaged pressure (force per total initial area) and number of turns for initiation of $\alpha \to \omega$ and $\alpha \to \beta$ PTs. That means that the system is considered as a black box. At the same time, the fields of pressure, plastic strain, and volume fraction of phases in the Zr sample during HPT, which are required for understanding actual physical, thermodynamic, and kinetic processes of interaction between PT and plasticity, are unknown.

In this paper, $\alpha \to \omega$ PT in Zr coupled to plastic flow under a fixed applied compressive force and torsion-induced large plastic shear strains in the RDAC are investigated by using FEM. Under the compression with the normal applied stress σ_n =27.6 MPa (corresponding to the

averaged pressure in a sample of 0.784 GPa), the sample thickness reduces by 44%. PT starts in the region near the symmetry plane in the center of the sample, where the maximum pressure exists. The maximum plastic strain is localized at the contact surface at the periphery due to a large shear deformation, but PT cannot occur there because the pressure is lower than the minimum pressure for strain-induced PT, p_{ε}^{d}. During the rotation of an anvil at fixed force, the radial shear (and twisting) stress increases at the center of a sample due to a stronger ω phase and corresponding to material hardening of the $\alpha+\omega$ phase mixture during PT, and the sample thickness reduces due to the material radial flow. This leads to a drastic increase in the pressure gradient and pressure at the center of sample. In this manner, we reproduced the pressure self-multiplication effect observed experimentally for other materials [8,9,11] with the stronger high-pressure phase. Thus, our prediction of this effect for $\alpha \rightarrow \omega$ PT in Zr is conceptually justified. With an increasing rotation angle, PT propagates from the center toward the periphery. In the major region, except at the center of a sample, the total contact friction stress τ is equal to the yield strength in shear, which means that the plastic sliding is allowed. Relative slip between the sample and the diamond increases, and the pace of thickness reduction decreases during rotation. Due to the radial material flow, the ω phase can be observed in the region where pressure is lower than the minimum pressure for strain-induced PT, p_{ε}^{d}, which may lead to misinterpretation of the experimental data for determination of the minimum PT pressure. Because the axial load is fixed, the region at the center of a sample with $p > p_{\varepsilon}^{d}$ does not essentially grow, imposing a limitation on the maximum mass of transformed material. Further increase in rotation is not effective because while there is some small increase in the amount of transformed material in the region with $p > p_{\varepsilon}^{d}$, thickness of this region reduces and reverse PT in the region with $p < p_{\varepsilon}^{r}$ is possible. To obtain a larger transformed region, a larger normal stress must be applied to increase the region with $p > p_{\varepsilon}^{d}$.

Although diamond is a very rigid material and the pressure is low, deformation of the diamond is not fully negligible due to its relatively large radial dimension. Thus, for a rotation angle of 0.8 and applied σ_n =27.6 MPa, the thickness of the sample at the center is 12.6 μm, and at the periphery (for r=100) it is 0.32 μm, or 2.5% smaller. This, in turn, affects the pressure distribution.

By comparison between the process with rotation and without rotation of an anvil, we find that the volume fraction of the ω phase is very small at the small normal applied load, but after torsion at the same load (i.e. the averaged pressure), a large transformed zone and volume fraction of the ω phase can be obtained. If an increase in the volume fraction of the ω phase in DAC is desired, the only way to produce plastic straining is to increase the applied load σ_n, which leads to higher pressure in both diamond and sample, in comparison to PT in the RDAC. This is the main reason for reporting the experimental PT pressure difference with and without torsion, e.g. in [32,33]. We would like to stress that the physics, mechanics, and kinetics of PT in DAC and RDAC are identical because we use the same equations and the same minimum PT

pressure p_{ε}^{d}. The difference is in the behavior of the system sample-loading device, which results in different pressure-accumulated plastic strain trajectories.

It is evident (e.g. from Fig. 3) that the PT process in RDAC, despite the potential advantage in comparison with DAC, is far from optimal. Thus, due to the much stronger high-pressure phase and pressure self-multiplication effect, the pressure in the transformed region is much higher than the minimum PT pressure p_{ε}^{d}. Such a high pressure is not required for PT but could not be avoided. The region in which PT occurs is limited by the condition $p > p_{\varepsilon}^{d}$ and cannot be increased by increasing the shear under a fixed force. A significant reduction in thickness during torsion also reduces the total mass of the high-pressure phase. A way to overcome these drawbacks is to place the sample within a strong gasket, optimize the geometric parameters of the gasket, and achieve nearly-homogeneous pressure distribution within the sample, which does not vary essentially during torsion and PT. This was achieved in experiments for PT from hexagonal to superhard wurtzitic boron nitride (based on a simplified analytical optimization) [7] and in FEM simulations in [23].

Similar to the PT under compression in DAC [26], obtained results for torsion in RDAC demonstrate that PT cannot be characterized by the averaged pressure, which is traditional in HPT. During torsion at the fixed averaged pressure, the maximum pressure grows from 1.8 GPa to 4.0 GPa (Fig. 10), i.e. by a factor of 2.2. This is slightly larger than a factor of 2, which was estimated in [26]. Further torsion leading to completion of PT at the center of a sample should lead to further increase in the maximum pressure. While the geometry of a sample in RDAC differs from that in the high-pressure torsion, some qualitative conclusions should be the same. Thus, under compression, the minimum pressure for the strain-induced PT p_{ε}^{d} =1.7 GPa is reached at the averaged pressure of 0.784 GPa, which is 2.2 times lower. It is lower than the upper bound of 3, estimated in [26], due to the effect of the part of the sample outside of the flat anvil surface, which is absent in the high-pressure torsion. This multiplier was used in [26] to correct the magnitude of p_{ε}^{d} pressure for $\alpha \rightarrow \omega$ PT based on the averaged pressure in [32,33]. The maximum pressure after torsion exceeds an averaged pressure of 0.784 GPa by a factor of 5. This factor should be used to correct the minimum pressure p_{ε}^{d} for $\alpha \rightarrow \beta$ PT based on the averaged pressure in [32,33]. Also, strong heterogeneity in all fields and difference in geometric conditions (which are very seldom specified), is one of the important sources of explanation of the strong scatter in transformation pressures for $\alpha \rightarrow \omega$ PT in Zr in [27-37].

The results obtained in this paper enhance understanding of the complex conditions under which strain-induced PT in the Zr sample occurs in the RDAC. They will be beneficial for the design of experiments and extraction of material parameters, as well as optimization and control of PTs by varying the geometry and loading conditions.

Acknowledgements

The support of ARO (W911NF-17-1-0225), NSF (DMR-1434613), ONR (N00014-16-1-2079), and Iowa State University (Vance Coffman Faculty Chair Professorship) is gratefully acknowledged.

Data availability

The raw/processed data required to reproduce these findings cannot be shared at this time as the data also forms part of an ongoing study.

References

[1] P.C. Burnley, H.W. Green, Stress Dependence of the Mechanism of the Olivine–Spinel Transformation, Nature, 338 (1989) 753–756.

[2] S.H. Kirby, Localized Polymorphic Phase Transformations in High-Pressure Faults and Applications to the Physical Mechanism of Deep Earthquakes, Journal of Geophysics Research, 92 (B13) (1978) 13789.

[3] T.C. Wu, W.A. Basset, P.C. Burnley, M.S. Weathers, Shear-promoted phase transitions in Fe2SiO4 and Mg2SiO4 and the mechanism of deep earthquakes. Journal of Geophysics Research, 98 (1993) 19767-19776.

[4] V.I. Levitas, Y. Ma, E. Selvi, J. Wu, J.A. Patten, High-density amorphous phase of silicon carbide obtained under large plastic shear and high pressure, Physical Review B, 85 (2012) 054114.

[5] C. Ji, V.I. Levitas, H. Zhu, J. Chaudhuri, A. Marathe, Y. Ma, Shear-Induced Phase Transition of Nanocrystalline Hexagonal Boron Nitride to Wurtzitic Structure at Room Temperature and Lower Pressure, Proceedings of the National Academy of Sciences, 109 (2012) 19108-19112.

[6] Y. Ma, E. Selvi, V.I. Levitas, J. Hashemi, Effect of Shear Strain on the α–ε Phase Transition of Iron: A New Approach in the Rotational Diamond Anvil Cell, Journal of Physics: Condensed Matter, 18 (2006) S1075.

[7] V.I. Levitas, Y. Ma, J. Hashemi, M. Holtz, N. Guven, Strain-Induced Disorder, Phase Transformations, and Transformation-Induced Plasticity in Hexagonal Boron Nitride Under Compression and Shear in a Rotational Diamond Anvil Cell: In Situ X-Ray Diffraction Study and Modeling, Journal of Chemical Physics, 125 (2006) 044507.

[8] V.D. Blank, E.I. Estrin, Phase Transitions in Solids under High Pressure, New York : CRC Press, 2014.

[9] V.D. Blank, Y.Y. Boguslavsky, M.I. Eremets, E.S. Itskevich, Y.S. Konyaev, A.M. Shirokov, E.I. Estrin, Pressure Self-Multiplication Effect on Phase-Transition under Quasi-Hydrostatic Conditions, Zhurnal Eksperimental'noi i Teoreticheskoi Fiziki (ISSN 0044-4510), In Russian, 87 (1984) 922-926.

[10] V.I. Levitas, High-pressure Mechanochemistry: Conceptual Multiscale Theory and Interpretation of Experiments, Physical Review B, 70 (2004) 184118.

[11] N.V. Novikov, S.B. Polotnyak, L.K. Shvedov, V.I. Levitas, Regularities of Phase Transformations and Plastic Straining of Materials in Compression and Shear on Diamond Anvils: Experiments and Theory, Journal of Superhard Materials, 21 (1999) 39-51.
[12] V.I. Levitas, L.K. Shvedov, Low-Pressure Phase Transformation from Rhombohedral to Cubic Bn: Experiment and Theory, Physical Review B, 65 (2002) 104109.
[13] V.I. Levitas, Continuum mechanical fundamentals of mechanochemistry in High-pressure surface science and engineering, Edited by Y. Gogotsi and V. Domnich, Institute of Physics Publishing, 2004.
[14] V. Blank, M. Popov, S. Buga, V. Davydov, A.N. Ivlev, B.N. Mavrin, R. Ceolin, H. Szwarc, A. Rassat, Is C60 Fullerite Harder than Diamond?, Physics Letters A, 188 (1994) 281-286.
[15] V.I. Levitas, M. Javanbakht, Phase Transformations in Nanograin Materials under High Pressure and Plastic Shear: Nanoscale Mechanisms, Nanoscale, 6 (2014) 162-166.
[16] M. Javanbakht, V.I. Levitas, Nanoscale Mechanisms for High-Pressure Mechanochemistry: A Phase Field Study, Journal of Materials Science, (2018) https://doi.org/10.1007/s10853-018-2175-x.
[17] V.I. Levitas, Phase Transformations under High Pressure and Large Plastic Deformations: Multiscale Theory and Interpretation of Experiments, Proceedings of the International Conference on Martensitic Transformations: Chicago (ICOMAT) 2017.
[18] B. Feng, V.I. Levitas, Y. Ma, Strain-Induced Phase Transformation under Compression in a Diamond Anvil Cell: Simulations of a Sample and Gasket, Journal of Applied Physics, 115 (2014) 163509.
[19] B. Feng, V.I. Levitas, O.M. Zarechnyy, Plastic Flows and Phase Transformations in Materials under Compression in Diamond Anvil Cell: Effect of Contact Sliding, Journal of Applied Physics, 114 (2013) 043506.
[20] B. Feng, O.M. Zarechnyy, V.I. Levitas, Strain-Induced Phase Transformations under Compression, Unloading, and Reloading in a Diamond Anvil Cell, Journal of Applied Physics, 113 (2013) 173514.
[21] V.I. Levitas, O.M. Zarechnyy, Modeling and Simulation of Strain-Induced Phase Transformations under Compression in a Diamond Anvil Cell, Physical Review B, 82 (2010) 174123.
[22] B. Feng, V.I. Levitas, Coupled Phase Transformations and Plastic Flows under Torsion at High Pressure in Rotational Diamond Anvil Cell: Effect of Contact Sliding, Journal of Applied Physics, 114 (2013) 213514.
[23] B. Feng, V.I. Levitas, Effects of Gasket on Coupled Plastic Flow and Strain-Induced Phase Transformations under High Pressure and Large Torsion in a Rotational Diamond Anvil Cell, Journal of Applied Physics, 119 (2016) 015902.
[24] B. Feng, V.I. Levitas, O.M. Zarechnyy, Strain-Induced Phase Transformations under High Pressure and Large Shear in a Rotational Diamond Anvil Cell: Simulation of Loading, Unloading, and Reloading, Computational Materials Science, 84 (2014) 404-416.

[25] V.I. Levitas, O.M. Zarechnyy, Modeling and Simulation of Strain-Induced Phase Transformations under Compression and Torsion in a Rotational Diamond Anvil Cell, Physical Review B, 82 (2010) 174124.
[26] B. Feng, V.I. Levitas, Plastic Flows and Strain-Induced Alpha to Omega Phase Transformation in Zirconium during Compression in a Diamond Anvil Cell: Finite Element Simulations, Materials Science and Engineering: A, 680 (2017) 130-140.
[27] A. Jayaraman, W. Klement, and G.C. Kennedy, Melting and Polymorphism at High Pressures in Some Group IV Elements and III-V Compounds with the Diamond/Zincblende Structure, Physical Review, 130 (1962) 540.
[28] V. A. Zilbershtein, G. I. Nosova, E. I. Estrin, Alpha--omega transformation in titanium and zirconium, Fizika Metallov I Metallovedenie 35 (1973) 584-589.
[29] V. A. Zilbershtein, N. P. Chistotina, A. A. Zharov, N. S. Grishina, E. I. Estrin, Alpha-omega transformation in titanium and zirconium during shear deformation under pressure, Fizika Metallov I Metallovedenie 39 (1975) 445-447.
[30] S.K. Sikka, Y.K. Vohra, R., Chidambaram, Omega Phase in Materials, Progress in Materials Science, 27 (1982) 245-310.
[31] H. Xia, S.J. Duclos, A.L. Ruoff, Y.K. Vohra, New High-Pressure Phase Transition in Zirconium Metal, Physical Review Letters, 64 (1991) 204-207.
[32] B. Srinivasarao, A.P. Zhilyaev, M.T. Perez-Prado, Orientation Dependency of the Alpha to Omega Plus Beta Transformation in Commercially Pure Zirconium by High-Pressure Torsion, Scripta Materialia, 65 (2011) 241-244.
[33] A.P. Zhilyaev, I. Sabirov, G. Gonzalez-Doncel, J. Molina-Aldareguia, B. Srinivasarao, M.T. Perez-Prado, Effect of Nb Additions on the Microstructure, Thermal Stability and Mechanical Behavior of High Pressure Zr Phases under Ambient Conditions, Materials Science and Engineering: A, 528 (2011) 3496-3505.
[34] B. Olinger, J. C. Jamieson, Zirconium: Phases and Compressibility to 120 Kilobars, High Temperatures High pressures, 5 (1973) 123-131.
[35] J.C. Jamieson, Crystal Structures of Titanium, Zirconium, and Hafnium at High Pressures, Science, 140 (1963) 72-3.
[36] K. Edalati, Z. Horita, S. Yagi, E. Matsubara, Allotropic phase transformation of pure zirconium by high-pressure torsion, Materials Science and Engineering: A, 523 (2009) 277–281.
[37] A.P. Zhilyaev, F. Gálvez, A. Sharafutdinov, M.T. Pérez-Prado, Influence of the high pressure torsion die geometry on the allotropic phase transformations in pure Zr, Materials Science and Engineering: A, 527 (2010) 3918–3928.
[38] M.T. Pérez-Prado, A.P. Zhilyaev, First Experimental Observation of Shear Induced hcp to bcc Transformation in Pure Zr, Physical Review Letters, 102 (2009) 175504.
[39] K. Edalati, Z. Horita, A review on high-pressure torsion (HPT) from 1935 to 1988, Materials Science and Engineering: A, 652 (2016) 325–352.
[40] M. Kamrani, V.I. Levitas, B. Feng, FEM simulation of large deformation of copper in the quasiconstrain. Materials Science and Engineering: A, 705, (2017), 219-230.

[41] R.J. Hemley, H.K. Mao, G.Y. Shen, J. Badro, P. Gillet, M. Hanfland, D. Hausermann, X-ray Imaging of Stress and Strain of Diamond, Iron, and Tungsten at Megabar Pressures, Science, 276 (1997) 1242-1245.
[42] V.I. Levitas, Large Deformation of Materials with Complex Rheological Properties at Normal and High Pressure. New York: Nova Science, 1996.
[43] ABAQUS V6.11. Providence RI, USA: ABAQUS INC, 2011.
[44] S.Q. Wang, H.Q. Ye, First-Principles Study on the Lonsdaleite Phases Of C, Si and Ge, Journal of Physics Condensed Matter, 15 (2003) L197-L202.
[45] E. Guler, M. Guler, Elastic and Mechanical Properties of Cubic Diamond under Pressure, Chinese Journal of Physics, 53 (2015) 040807-1-11.
[46] B.T. Wang, P. Zhang, H.Y. Liu, W.D. Li, P. Zhang, First-Principles Calculations of Phase Transition, Elastic Modulus, and Superconductivity under Pressure for Zirconium, Journal of Applied Physics, 109 (2011) 063514.
[47] Y.S. Zhao, J.Z. Zhang, Enhancement of Yield Strength in Zirconium Metal through High-Pressure Induced Structural Phase Transition, Applied Physics Letters, 91 (2007) 201907.
[48] C.W. Greeff, Phase Changes and the Equation of State of Zr, Modelling and Simulation in Materials Science and Engineering, 13 (2005) 1015-1027.
[49] V.I. Levitas, O.M. Zarechnyy, Numerical Study of Stress and Plastic Strain Evolution under Compression and Shear of a Sample in a Rotational Anvil Cell, High Pressure Research, 30 (2010) 653-669.